

Navier–Stokes Simulation of Harmonic Point Disturbances in an Airfoil Boundary Layer

Christian Stemmer,* Markus J. Kloker,† and Siegfried Wagner‡
University of Stuttgart, 70550 Stuttgart, Germany

Laminar-turbulent transition mechanisms induced by a harmonic point source disturbance in a flat-plate boundary layer with adverse pressure gradient are investigated by fourth-order accurate spatial direct numerical simulation based on the complete three-dimensional Navier–Stokes equations for incompressible flow. The disturbance is introduced into the two-dimensional base flow by time-periodic simultaneous blowing and suction within a circular spot at the wall to quietly mimic the momentum input by an active loudspeaker below a hole in the surface in respective experiments. Thus a wave train consisting of pure Tollmien–Schlichting waves of a single frequency and a large number of obliqueness angles is stimulated, and its downstream evolution in both physical and spectral space is investigated. A breakdown scenario dominated entirely by oblique modes is observed that shows a spanwise peak/valley amplitude splitting with the valley plane at the centerline of the wave train. Dominant vorticity structures develop off centerline, and a clear-cut \mathcal{M} -shaped structure is formed in final stages related to the wall shear being a footprint of a first pair of Λ -vortices in the flow.

Nomenclature

\tilde{f}	= dimensional disturbance frequency
H_{12}	= shape factor, $H_{12} = \delta_1 / \delta_2$
h	= multiple of the disturbance frequency
(h, k)	= disturbance mode with frequency $h\beta$ and spanwise wave number $k\gamma$
k	= multiple of the basic spanwise wave number
\tilde{L}	= reference length scale
R	= radius of the point source
Re_{δ_1}	= Reynolds number based on the displacement thickness
\tilde{U}_∞	= reference velocity
u_e	= normalized velocity at the boundary layer edge
u, v, w	= velocity in the streamwise, wall normal, spanwise direction
x, y, z	= streamwise, wall normal, spanwise direction
α_i	= spatial amplification rate, $-(d/dx) \ln(A/A_0) = -1/A \cdot dA/dx$
β	= nondimensional angular disturbance frequency, $\tilde{f} \cdot 2\pi \cdot \tilde{L} / \tilde{U}_\infty, 9.449$
γ	= basic spanwise wave number, 3.3
δ_1	= boundary-layer displacement thickness
δ_2	= boundary-layer momentum thickness
θ	= obliqueness angle of disturbance waves with respect to the x direction
λ_z	= spanwise width of the integration domain
$\tilde{\nu}$	= kinematic viscosity
ω	= disturbance vorticity

Subscript

B = baseflow quantities

Superscripts

, = disturbance quantities
~ = dimensional quantities

Presented as Paper 98-2436 at the AIAA 29th Fluid Dynamics Conference, Albuquerque, NM, 15–18 June 1998; received 30 September 1998; revision received 25 January 2000; accepted for publication 25 January 2000. Copyright © 2000 by the authors. Published by the American Institute of Aeronautics and Astronautics, Inc., with permission.

*Research Assistant, Institut für Aero- und Gasdynamik, Pfaffenwaldring 21; stemmer@iag.uni-stuttgart.de. Member AIAA.

†Research Scientist, Institut für Aero- und Gasdynamik, Pfaffenwaldring 21.

‡Professor, Aero- and Gasdynamics, Institut für Aero- und Gasdynamik, Pfaffenwaldring 21. Member AIAA.

I. Introduction

THE investigation of laminar-turbulent transition has engaged many researchers over the past decades. A fundamental step toward the understanding of laminar breakdown of a two-dimensional zero-pressure-gradient (ZPG) boundary layer at low background disturbance level was attained through Klebanoff et al. (see Ref. 1) in the early 1960s. They described the so-called fundamental breakdown (K -breakdown), which is dominated by the presence of a two-dimensional Tollmien–Schlichting (TS) wave with an amplitude higher than 1–2% u'/u_e . The resonant interaction with a pair of symmetrically oblique three-dimensional waves with the same frequency but lower amplitude at first, and a longitudinal vortex system leads to breakdown with the appearance of aligned lambda-shaped (Λ -)vortices. This was believed to be the fundamental path to transition up to the discovery of a subharmonic resonance mechanism. The resonance of a two-dimensional wave and a pair of symmetrically oblique three-dimensional waves of half the frequency, getting active at a two-dimensional wave threshold amplitude about five times lower than in the fundamental case, leads to breakdown with a staggered arrangement of Λ -vortices. Kachanov et al. of Novosibirsk (see Ref. 1) observed this transition type experimentally in a flat-plate boundary layer and it is referred to as N -breakdown or H -breakdown owing to Herbert's work on secondary instability.¹ In 1991, a third basic path to transition with no dominant two-dimensional wave was discovered through direct numerical simulations (DNS), at first for transonic boundary layers, by Thumm² and Fasel et al.³ A growing pair of symmetrically oblique three-dimensional waves triggers this kind of transition, which is accompanied by a strong steady mode with doubled spanwise wave number and it was named oblique breakdown and verified also for incompressible flow (see, e.g., Ref. 4). Recently, slender Λ -vortices could be observed here.

The present study deals with a two-dimensional boundary layer present on an airfoil at considerable angle of attack including an extended region of adverse pressure gradient (APG). DNS studies on a Falkner–Skan-type boundary layer near separation (Hartree parameter $\beta_h = -0.18$) by Kloker^{5,6} indicate that, among the classical breakdown scenarios discussed, the fundamental K type is the most “dangerous.” Compared to ZPG flows, however, the disturbance growth is much more intense because of additional inviscid instability that is present only in APG conditions with inflectional base flow $u_B(y)$ profiles. The final breakdown process differs from the ZPG K -type dynamics considerably. A timewise periodically generated zone of local flow separation gives rise to a secondary system of tightly parallel longitudinal vortices in between neighboring Λ -vortices. This vortex system rapidly decays into many

hairpin vortices, thus precipitating ultimate breakdown of the APG laminar flow.

A step further toward the understanding of transition mechanisms induced by more complex boundary/initial conditions is the involvement of numerous oblique waves of, at first, a single frequency. The harmonic point source (HPS) generates, by its spatial localization, a full spectrum of symmetrically oblique disturbance waves, including a plane wave, with well-defined initial amplitude and phase relations. Moreover, it can be thought of as a model for the generation of disturbances by a localized stationary surface roughness and a sound wave. Seifert and Wagners⁷ and Seifert⁸ experimentally investigated the HPS disturbance development in ZPG and mild APG flow, finding good agreement with predictions by linear stability theory if the base flow is accurately controlled and documented in the experiment. Regarding the nonlinear development and breakdown, the growth of (background) subharmonic components has been observed as well. The role of the subharmonic disturbance components, however, can strongly depend on the amplitude level of the background noise (or disturbance generator noise) and the basic breakdown mechanism. Under the experimental conditions, the onset of breakdown had been seen first on the disturbance centerline. For clarification of these findings, DNS is an ideal tool because the flow conditions and the disturbance input are completely controlled.

The HPS has also been chosen as the reference disturbance source for the validation of the experimental setup of a national joint research project. The goal is to measure and investigate transition phenomena in flight. Comparisons of DNS results discussed in this paper with in-flight experiments carried out by four other German universities [Rheinisch Westfälische Technische Hochschule Aachen (RWTH Aachen), Technische Universität Berlin (TU Berlin), Technische Hochschule Darmstadt (TH Darmstadt), and University Erlangen] using respective wing gloves for a research motor glider can be found in Refs. 9 and 10.

II. Numerical Method

The numerical model is based on the complete Navier-Stokes equations for incompressible, three-dimensional unsteady flow in the vorticity-velocity formulation.^{5,6,11,12} The equations are solved in a disturbance formulation. For this purpose, the system is split in a two-dimensional steady base flow (denoted by the index B) and the three-dimensional unsteady disturbance flow (denoted by a prime). Thus,

$$\begin{aligned} u &= u_B + u', & v &= v_B + v', & w &= w' \\ \omega_x &= \omega'_x, & \omega_y &= \omega'_y, & \omega_z &= \omega_{z_B} + \omega'_z \end{aligned} \quad (1)$$

The utilized variables are nondimensionalized:

$$\begin{aligned} x &= \tilde{x}/\tilde{L}, & y &= (\tilde{y}/\tilde{L})\sqrt{Re}, & z &= \tilde{z}/\tilde{L}, & t &= \tilde{t}(\tilde{U}_\infty/\tilde{L}) \\ u &= \tilde{u}/\tilde{U}_\infty, & v &= (\tilde{v}/\tilde{U}_\infty)\sqrt{Re}, & w &= \tilde{w}/\tilde{U}_\infty \end{aligned} \quad (2)$$

with the reference Reynolds number defined as $Re = \tilde{U}_\infty \tilde{L}/\tilde{\nu}$. Variables with a tilde denote dimensional variables. Here, $Re = 14.8 \times 10^4$ with $\tilde{U}_\infty = 38.9$ m/s. The reference length is $\tilde{L} = 0.065$ m, which corresponds to the chord of the wing glove by a factor of $1/20$ (chord = $20 \times \tilde{L}$).

The three nondimensional vorticity components are defined as follows:

$$\begin{aligned} \omega_x &= \frac{1}{Re} \frac{\partial v}{\partial z} - \frac{\partial w}{\partial y}, & \omega_y &= \frac{\partial w}{\partial x} - \frac{\partial u}{\partial z}, \\ \omega_z &= \frac{\partial u}{\partial y} - \frac{1}{Re} \frac{\partial v}{\partial x} \end{aligned} \quad (3)$$

The simulation is carried out in a rectangular integration domain (Fig. 1) that includes a disturbance strip for the disturbance introduction. First, the steady two-dimensional base flow is calculated using the Navier-Stokes equations with a prescribed streamwise velocity distribution at the upper boundary. Second, the disturbances are introduced and the three-dimensional disturbance flow is calculated.

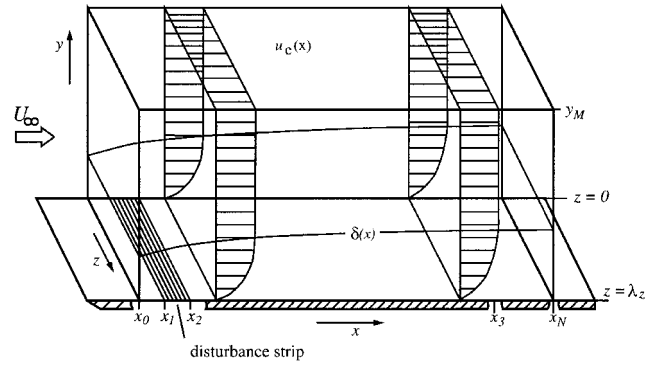


Fig. 1 Integration domain with disturbance strip.

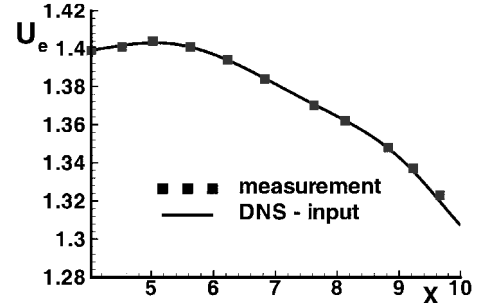


Fig. 2 Velocity distribution at the upper boundary of the integration domain; squares: measurement; —, least-squares spline fit.

A. Calculation of the Base Flow

The accompanying experiments delivered the pressure distribution on the airfoil. The streamwise velocity at the upper domain boundary ($u_e(x)$) is deduced from Bernoulli's equation. The $u_e(x)$ distribution is shown in Fig. 2, where the line represents a least-squares spline fit to the measured values. With a pseudotemporal technique (implicitly in x , explicitly in y), a solution to the steady vorticity-transport equation

$$\frac{\partial}{\partial x}(u_B \omega_{z_B}) + \frac{\partial}{\partial y}(v_B \omega_{z_B}) = \frac{1}{Re} \frac{\partial^2 \omega_{z_B}}{\partial x^2} + \frac{\partial^2 \omega_{z_B}}{\partial y^2} \quad (4)$$

can be calculated with Poisson-type equations for u_B and v_B

$$\frac{\partial^2 u_B}{\partial x^2} = -\frac{\partial^2 v_B}{\partial x \partial y} \quad (5)$$

$$\frac{1}{Re} \frac{\partial^2 v_B}{\partial x^2} + \frac{\partial^2 v_B}{\partial y^2} = -\frac{\partial \omega_{z_B}}{\partial x} \quad (6)$$

The boundary conditions for the steady base flow are no-slip conditions at the wall and vanishing vorticity and prescribed $u_e(x)$ at the upper boundary $y = y_M$ with $\partial v_B / \partial y = -\partial u_e / \partial x$. Here the influence of the height y_M using a fixed $u_e(x)$ distribution is negligibly small. At the inflow boundary, an appropriate local Falkner-Skan similarity solution is used, derived from the local shape factor H_{12} . At the outflow boundary, all equations are solved dropping the second x -derivative terms, and u_B is calculated from $\partial^2 u_B / \partial y^2 = \partial \omega_{z_B} / \partial y$.

The Reynolds number based on the laminar displacement thickness is $Re_{\delta_1}(x=4) = 1335$ at the inflow boundary and $Re_{\delta_1}(x=9) = 2953$. Downstream of $x=9$, the measured APG (see Fig. 2) increases and the laminar base flow tends to separate. The shape factor H_{12} (Fig. 3) exceeds the value of 4.0 above which separation occurs. To assure the base flow calculation to converge to a physically existing steady state, a zone of acceleration has been appended downstream of $x=10$ ranging to $x_N = 11.8$ with $\Delta u_e = 0.012$. This secures the laminar bubble to keep short and thus to remain steady and to be closed before $x = x_N$. Re_{δ_1} and H_{12} are shown in Fig. 3 for the steady laminar base flow (two-dimensional steady Navier-Stokes) and the disturbed flow (averaged in z and t direction; three-dimensional unsteady DNS) as discussed later. The decrease in Re_{δ_1}

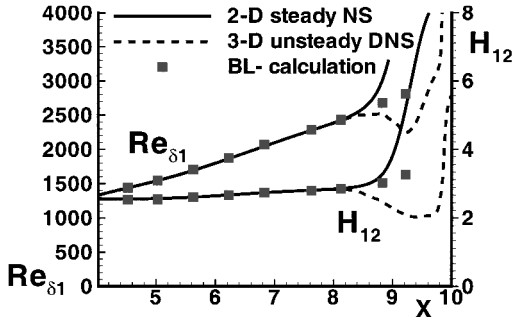


Fig. 3 Streamwise evolution of integral values: BL, boundary layer calculation with transition fixed at $x = 9.0$.

as well as in H_{12} at $x = 9.0$ is typical for transition. H_{12} does not come close to the threshold value for separation because the turbulent boundary layer can follow a much stronger APG without separating. For the investigated pressure gradient and disturbance input, transition occurs before laminar separation can occur.

B. Calculation of the Disturbance Flow

For the simulation of the unsteady flow, the set of three disturbance–vorticity transport equations

$$\begin{aligned} \frac{\partial \omega'_x}{\partial t} + \frac{\partial}{\partial y}(v' \omega'_x - u' \omega'_y + v_B \omega'_x - u_B \omega'_y) \\ - \frac{\partial}{\partial z}(u' \omega'_z - w' \omega'_x + u_B \omega'_z + u' \omega_{zB}) &= \Delta^* \omega'_x \\ \frac{\partial \omega'_y}{\partial t} - \frac{\partial}{\partial x}(v' \omega'_x - u' \omega'_y + v_B \omega'_x - u_B \omega'_y) \\ + \frac{\partial}{\partial z}(w' \omega'_y - v' \omega'_z - v_B \omega'_z - v' \omega_{zB}) &= \Delta^* \omega'_y \\ \frac{\partial \omega'_z}{\partial t} + \frac{\partial}{\partial x}(u' \omega'_z - w' \omega'_x + u_B \omega'_z + u' \omega_{zB}) \\ - \frac{\partial}{\partial y}(w' \omega'_y - v' \omega'_z - v_B \omega'_z - v' \omega_{zB}) &= \Delta^* \omega'_z \end{aligned} \quad (7)$$

has to be solved.

For the disturbance velocities u' , v' , w' three Poisson-type equations have to be solved:

$$\frac{\partial^2 u'}{\partial x^2} + \frac{\partial^2 u'}{\partial z^2} = -\frac{\partial \omega'_y}{\partial z} - \frac{\partial^2 v'}{\partial x \partial y} \quad (8)$$

$$\Delta^* v' = \frac{\partial \omega'_x}{\partial z} - \frac{\partial \omega'_z}{\partial x} \quad (9)$$

$$\frac{\partial^2 w'}{\partial x^2} + \frac{\partial^2 w'}{\partial z^2} = \frac{\partial \omega'_y}{\partial x} - \frac{\partial^2 v'}{\partial y \partial z} \quad (10)$$

where the modified Laplacian Δ^* is defined as

$$\Delta^* = \frac{1}{Re} \frac{\partial^2}{\partial x^2} + \frac{\partial^2}{\partial y^2} + \frac{1}{Re} \frac{\partial^2}{\partial z^2} \quad (11)$$

At the upper boundary ($y = y_M$), potential flow holds:

$$\omega'_x|_{y=y_M} = \omega'_y|_{y=y_M} = \omega'_z|_{y=y_M} = 0 \quad (12)$$

For v' , the local wall-normal gradient is prescribed:

$$\left. \frac{\partial v'}{\partial y} \right|_{y=y_M} = -\frac{\alpha^*}{\sqrt{Re}} v'|_{y=y_M} \quad (13)$$

where α^* can be thought of as a streamwise wave number of the disturbance (cf. linear stability theory). For simulation of late transitional stages with mean flow distortion, α^* is typically set to zero.

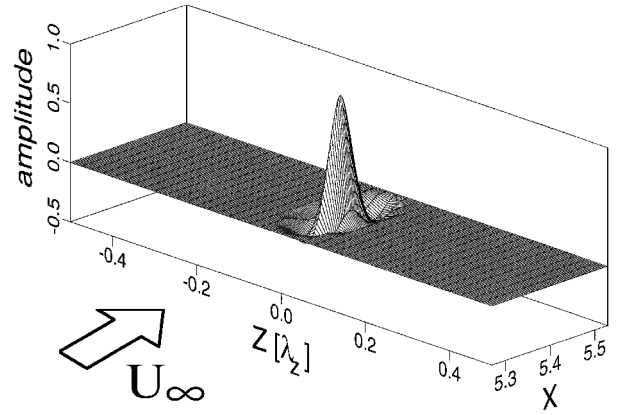


Fig. 4 Wall-normal velocity v' distribution across the disturbance strip over one spanwise wavelength λ_z .

The no-slip condition for u' and w' is satisfied at the wall ($y = y_0$); v' is also zero except for the disturbance strip (Fig. 4), where the disturbance function for the HPS is prescribed. The function is designed such that, at any time step of the excitation cycle, only momentum but no net mass flow is introduced, and hence the generation of sound is minimized, facilitating TS wave analysis:

$$v'(x, y = 0, z, t) = f_v(x, z) \cdot \sin(\beta t + \varphi_0)$$

$$f_v(x, z) = A \{14q^5 - 45q^4 + 50q^3 - 20q^2 + 1\} \quad (14)$$

r is the actual distance to the point source center $r^2 = x^2 + z^2$, and the radius of the point source is $R = 0.1309$; the value q is built by $q = r/R$ ($0 \leq q \leq 1$). For the wall vorticities ω'_x , ω'_z special equations are used.^{11,12}

The disturbances are introduced well downstream of the inflow boundary of the rectangular integration domain, which permits us to force all disturbance variables to be zero at the inflow boundary.

As for the outflow boundary conditions, the implementation of the well-tested method of “artificial relaminarization”¹¹ is applied, where basically the three disturbance vorticity components are gradually forced to a zero value in a damping domain ($x_3 \leq x \leq x_4$, $x_4 \leq x_N$ in Fig. 1). At $x = x_N$, the solution of Eq. (9), dropping the second x -derivative term, is $v'(y) = 0$. The $u'(y)$ and $w'(y)$ distributions at $x = x_N$ are computed by integrating the definitions (3) for $k > 0$, and for $k = 0$, $u'(x, y)$ is integrated starting from $x = x_0$, employing the continuity equation.

In spanwise direction, periodic boundary conditions for all disturbance components $f \in \{u', v', w', \omega'_x, \omega'_y, \omega'_z\}$ and their derivatives are enforced:

$$f'|_{z=0} = f'|_{z=\lambda_z}, \quad \left. \frac{\partial^n f'}{\partial z^n} \right|_{z=0} = \left. \frac{\partial^n f'}{\partial z^n} \right|_{z=\lambda_z} \quad (15)$$

C. Discretization and Numerics

The numerical method employs a Fourier spectral representation of the spanwise spatial dimension z . All variables are represented through

$$f'(x, y, z, t) = \sum_{k=-K}^K F_k(x, y, t) e^{ik\gamma z} \quad (16)$$

where $k\gamma$ is referred to as the spanwise wave number. The basic spanwise wave number γ for the fundamental Fourier mode ($k = 1$) is related to the spanwise width λ_z of the integration domain through $\gamma = 2\pi/\lambda_z$, here $\gamma = 3.3$. The considered flowfield is symmetric with respect to $z = 0$ and hence all F_k are purely real for u' , v' , and ω'_z and purely imaginary for w' , ω'_x , and ω'_y .

The modeled point source (as seen in Fig. 4) is Fourier analyzed in spanwise direction for every x location $x_1 \leq x \leq x_2$ and the resulting amplitudes for symmetrical pairs of three-dimensional waves with a large number of discrete spanwise wave numbers ($k\gamma$) are taken as disturbance input. The Fourier amplitudes are shown in

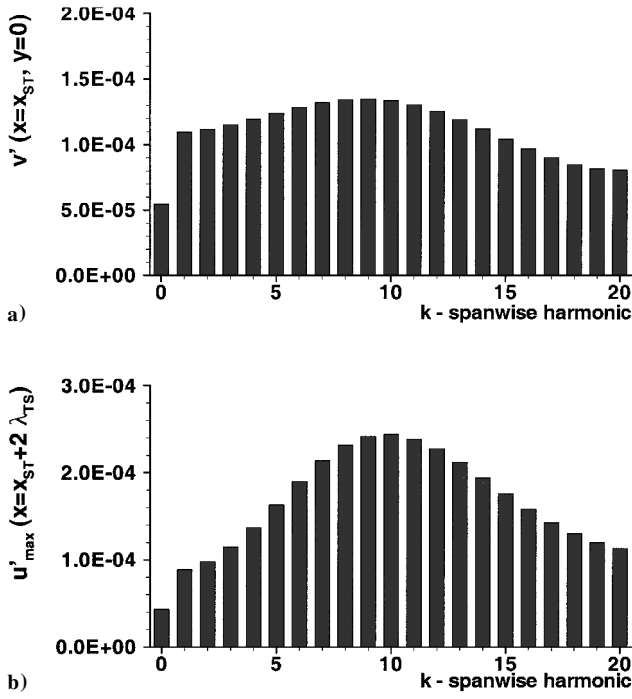


Fig. 5 Fourier amplitudes of the a) velocity v' at the disturbance strip center, $x = 5.4$; and b) y maximum of u' two average TS wavelengths downstream of the disturbance strip.

Fig. 5 for the center of the disturbance strip in x direction. The three-dimensional v' -disturbance input amplitudes ($k > 0$ and $k < 0$ added) have a maximum at $k = 9$ and decay monotonously for higher k , whereas the two-dimensional amplitude roughly is just half the average three-dimensional value. Because of the varying receptivity with respect to waves with different spanwise wave numbers, differing disturbance amplitudes for different obliqueness angles (θ) result inside the boundary layer. The lower graph in Fig. 5 shows the resulting u' amplitudes as obtained by a Fourier analysis in time roughly two average TS wavelengths downstream of the disturbance strip, when the TS waves have fully developed ($x = 5.7$). The two-dimensional wave (1, 0) (the first index gives multiples of the disturbance frequency β , the second multiples of the basic spanwise wave number γ) now is clearly smaller than one-half the smallest three-dimensional component ($k = 1$). From here on, the symmetrical wave pair ($h, \pm k$) is denoted as (h, k) and referred to as one three-dimensional wave with the amplitude corresponding to the sum of the left and right running wave. The u' amplitudes of the three-dimensional waves at $x = 5.7$ increase with ascending k up to $k = 10$ ($\theta \sim 54$ deg). Clearly, the receptivity of the boundary layer is largest for a wave angle of 54 deg, and for the two-dimensional wave ($k = 0$) the receptivity is smaller than for $k = 20$ ($\theta \sim 77$ deg). The radius of the point source covers about one-fifteenth of the spanwise wavelength λ_z and one-half the average streamwise TS wavelength λ_x , and is larger than the circle of holes used in the flight experiments. However, this does not affect the results.

The well-proven numerical method employs fourth-order finite-differences in the streamwise direction (unconditionally alternating upwind/downwind/central differences for the convective terms) and wall-normal direction and a fourth-order Runge-Kutta scheme for the time integration.^{5,6} The nonlinear terms are evaluated pseudospectrally using de-aliasing. The uniform equidistant grid for the point source problem contained at first $2354 \times 161 \times 40$ points in (x, y, z) directions. The problem was solved on a NEC SX-4/32 vector-supercomputer on 11 processors and a CRAY T3E-512 for a calculation with $K = 93$ and 234 Fourier modes (186, 468 points at least) in spanwise direction, using corresponding number of processors. A single calculation on the NEC SX-4/32 took about $3.5 \mu s$ per gridpoint and time step on a single processor with 700 time steps per fundamental disturbance period.

Grid refinement studies showed that, aside from the number of spanwise modes in the late stages, the x discretization is the crucial

point in resolution requirements. In the high resolution case, the grid spacing was $\Delta x = 0.00164$, $\Delta y = 0.1858$, and $\Delta z = 0.00407$, where appropriate data from a coarser run were used as unsteady inflow conditions. The flow structures as discussed in Sec. III are largely independent of the numerical parameters when the given values are used as a basis.

Because of the periodic boundary conditions in spanwise direction, a spanwise series of point sources is actually modeled with this approach. Therefore, the integration domain should be wide enough to largely inhibit the developing wave trains to interact with each other, resulting in a rather small basic spanwise wave number. With this small wave number, resolution toward the three-dimensional modes with high obliqueness angles (high spanwise wave number) becomes crucial to capture the behavior of the wave train in late transitional stages. The high spanwise resolution simulation showed that the wave train developing does not “leave” the integration domain on the sides.

III. Numerical Results

A. Primary Stability Properties

The steady base flow was analyzed for its stability properties with the linear stability theory (numerical solution of the Orr-Sommerfeld equation, spatial approach). In Fig. 6a, the stability diagram for two-dimensional modes is presented. The location of the disturbance strip ($5.3 \leq x \leq 5.5$) for the chosen frequency $\beta = 9.449$ ($f = 900$ Hz) is well inside the instability region ($\alpha_i < 0$). This frequency was chosen such that the largest amplification could be expected in the presumed area of breakdown ($8.0 \leq x \leq 9.0$). In the experiments, this frequency was adopted.¹⁰

The stability diagram for three-dimensional waves with spanwise wave numbers covered by the low-resolution calculation ($K = 20$) is displayed in Fig. 6b for $x = 5.7$ (vertical line in Fig. 6a). The amplification rates for waves up to an obliqueness angle of ≈ 37 deg ($k\gamma = 20$) are of comparable magnitude. The slightly larger amplification rates of the low k waves cannot make up for their lower initial amplitudes as can be seen in the downstream amplitude development in Fig. 7 (see also Fig. 5). This is especially significant for the two-dimensional wave. At the beginning of the strong nonlinear stage ($x \sim 8.0$ Fig. 7), all three-dimensional disturbance waves with

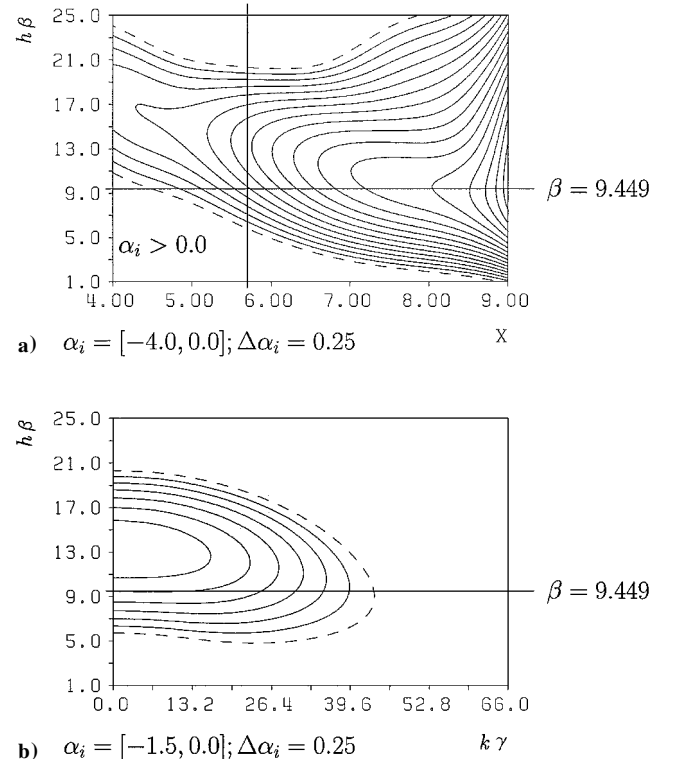


Fig. 6 Boundary-layer stability diagrams obtained by spatial linear stability theory: ---, neutral curve ($\alpha_i = 0$); a) α_i over $h\beta$ and x for two-dimensional waves ($\gamma = 0$) and b) α_i over $h\beta$ and $k\gamma$ at $x = 5.7$.

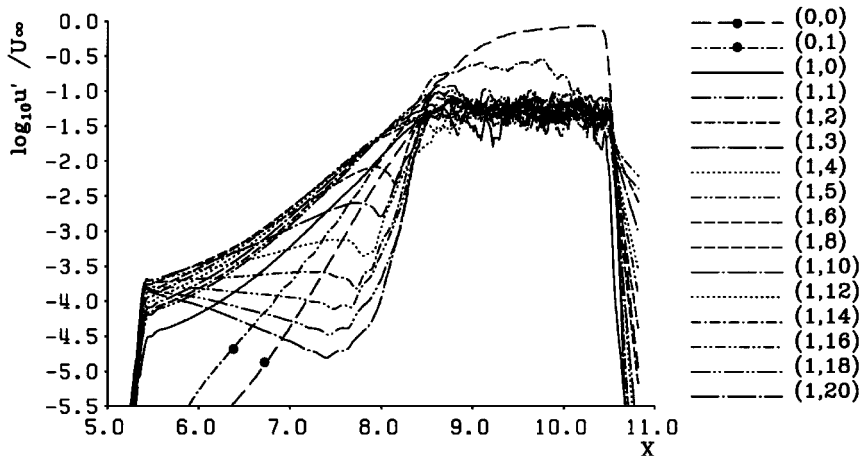


Fig. 7 Downstream amplitude development (maximum over y) of various modes in the frequency: spanwise wave number spectrum.

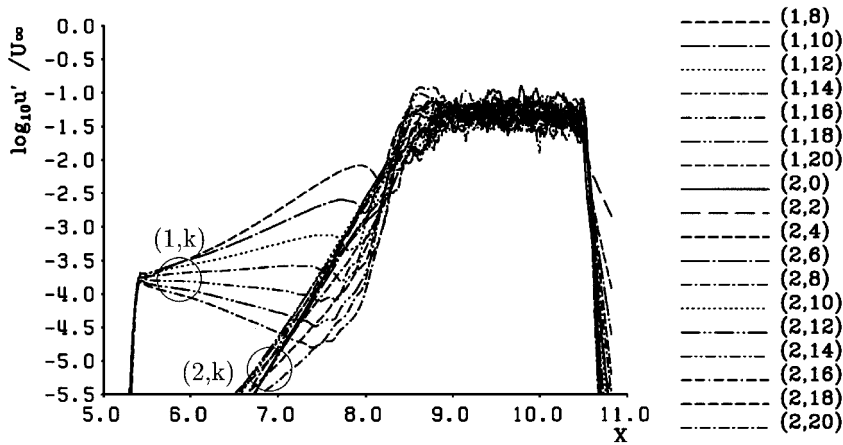


Fig. 8 Downstream amplitude development (maximum over y) of modes $(1, k)$, $8 \leq k \leq 20$, and modes $(2, k)$. Only even k are shown.

an obliqueness angle $\theta \leq 45$ deg ($k=6$) reach the same amplitude of $2\% u' / U_\infty$. The waves with higher obliqueness angles ($\theta > 45$ deg) are amplified much less in the quasi-linear disturbance stage and even attenuate for very high angles ($\theta > 60$ deg, $k > 14$) as can be anticipated taking into account Fig. 6b. Comparisons of DNS data with results of linear stability theory calculations and experimental data can be found in Ref. 13.

B. Early Nonlinear Stage in Fourier Space

Because the amplitudes of many three-dimensional waves are larger than the two-dimensional wave amplitude, a classical resonance mechanism is unlikely. Rather a kind of oblique breakdown in multiple fashion is conceivable at first. In this case, the modes $(0, 2k)$, $k=1-6$, should be large here. Compared to this extrapolation from standard oblique breakdown with one dominant wave pair $(1, 1)$, however, here the spectrum of $(1, k)$ modes generates a strong $(0, 1)$ mode that is not present in the one-wave-pair case and that is larger than any other $(0, k)$ mode, $k > 1$. We note that, because of quadratic nonlinearity [see Eq. (7)], the two modes $(h_1, k_1) \cdot (h_2, k_2)$ generate the modes $(|h_1 \pm h_2|, |k_1 \pm k_2|)$. Indeed, here the primary modes $(1, k)$, $k=0-K$, directly generate the full spectra $(0, k)$ and $(2, k)$, $k=0-K$. The higher harmonics $(2, k)$ subsequently act back on the full primary $(1, k)$ spectrum. Therefore, the modes $(1, k)$, $8 \leq k \leq 20$, strongly grow downstream of $x=7.5$, where the corresponding $(2, k)$ modes exceed the respective primary $(1, k)$ amplitudes (Fig. 8).

C. Simulation with Removal of Two-Dimensional Components

To substantiate the minor importance of the two-dimensional components for the observed transition scenario, two DNS were carried out with 1) $(1, 0)$ removed from the disturbance input and 2)

$(2, 0)$ filtered out during the simulation. In case 1, the downstream development of the unsteady three-dimensional modes (Fig. 9) basically shows the same behavior as in the case with two-dimensional input. The steady disturbance components $((0, 0)$ and $(0, 1))$ are marked with a filled circle in Figs. 7 and 9. The mode $(0, 0)$, representing the distortion in the two-dimensional mean flow, is not modified by the lack of the two-dimensional mode input up to $x=8.5$, where the flow already is in the quasi-turbulent regime, whereas the growth of the steady $(0, 1)$ mode is slightly delayed. As $(1, 0)$ is not disturbed in case 1, the nonlinear $(0, 1)$ generation is slightly weaker because of the missing generation through $(1, 0) \cdot (1, 1)$. However, $(1, 0)$ is nonlinearly generated by $(h, k) \cdot (h+1, k)$ and obtains relevant values downstream of $x=8.1$. Further detailed comparison also in physical space with the reference case does not show any significant difference in the two cases. In case 2, a subharmonic resonance mechanism with respect to the modes $(1, k)$, $k > 6$, triggered by $(2, 0)$ should be checked (see Fig. 8). To this end, $(2, 0)$ had been continuously filtered out numerically in space during a simulation with $(1, 0)$ input. The $(2, 0)$ amplitude thus was lowered by 1~2 orders of magnitude, but the behavior of the $(1, k)$ modes was identical. Hence, the HPS-breakdown scenario is clearly dominated by various three-dimensional mode interactions [$(1, k)$ and $(2, k)$ mainly] with strong $(0, 1)$ generation. Two-dimensional modes do not play any leading role, rather they are a side effect.

D. Depiction in Physical Space

The behavior of the wave train can be studied by means of Fig. 10, which shows lines of corresponding phases of fluctuations ω_i^t for the disturbance frequency at the wall. The time signal was Fourier analyzed over one disturbance cycle to obtain the Fourier phases of the fluctuations. The left margin of the picture marks the downstream

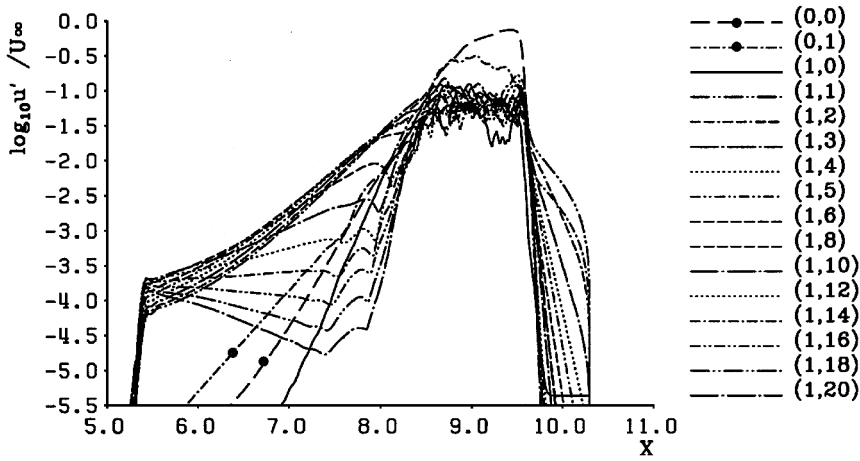


Fig. 9 Downstream amplitude development (maximum over y) of various modes in the frequency–spanwise wave number spectrum without initial two-dimensional disturbance input.

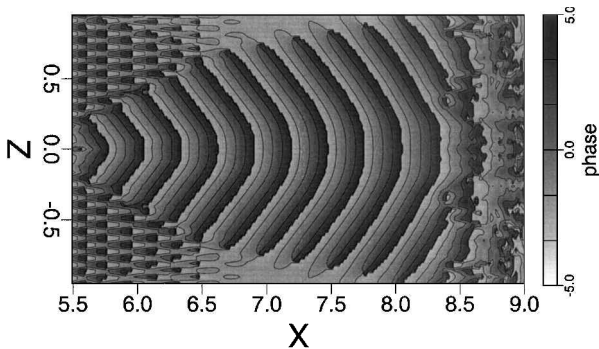


Fig. 10 Lines of constant phase of ω'_z at the wall (x - z plane) as obtained from a Fourier analysis for the disturbance frequency $\beta = 9.449$.

end of the disturbance strip. The boomerang shaped phase distribution just after the introduction of the disturbances has qualitatively been observed by Gilyov et al.,¹⁴ Seifert and Wagnanski,⁷ experimentally, and Mack and Herbert¹⁵ theoretically for ZPG flow. Curved wave fronts with a straightened middle part are formed. The regular pattern in spanwise direction beside the wave train for $5.5 \leq x \leq 6.6$ is an effect of the spectral cutoff at $K = 20$. Note, however, that the amplitude level can vary over several orders of magnitude in this plot. The waves with large k decline in amplitude because of the primary stability properties described in Sec. III.A. Thus, a high spanwise resolution of the point source itself eventually does not lead to different results. Downstream of $x = 6.5$, the typical wave train has fully developed and exhibits a half opening angle to the centerline of 12 deg, which is similar to the value observed in Blasius flow and is found in the joint experiments as well. The center region of the wave train straightens downstream of $x \sim 7.5$. As the development becomes increasingly nonlinear, this shape deformation becomes more pronounced ($x > 8.0$). The sharply defined wave front shape dissolves for $x > 8.5$ where the region of rapid final breakdown begins and higher harmonic frequency components are nonnegligibly large (recall the increasing APG; Fig. 3). The saturation of the amplitudes of the disturbance waves (Fig. 7) can be observed at the same downstream location.

To investigate the spanwise development of the disturbance intensity, the u' rms amplitudes are shown in Fig. 11. The development of u' rms on the centerline ($z = 0$) is surpassed by that at $z = 0.095$ and 0.19 . The centerline u' fluctuations are not the most intensive fluctuations in the area of transition ($x > 8.0$).

The transitional regime, where disturbance waves of large obliqueness angles reach amplitudes beyond 1% u'/U_∞ and detailed structures can be visualized experimentally, is limited to about one to two TS wavelengths. For the comparison with the experimental results, patterns of the instantaneous total wall-vorticity ω_z distribution from the simulation with $K = 93$ are evaluated, delivering

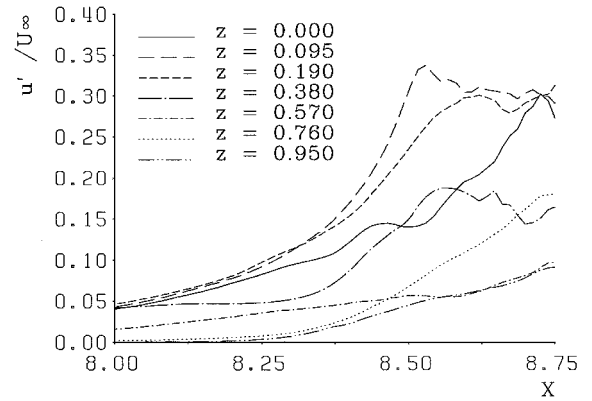


Fig. 11 u' -rms amplitudes (maximum over y) vs x for various spanwise positions ($z = 0.95 \approx \lambda_z/2$).

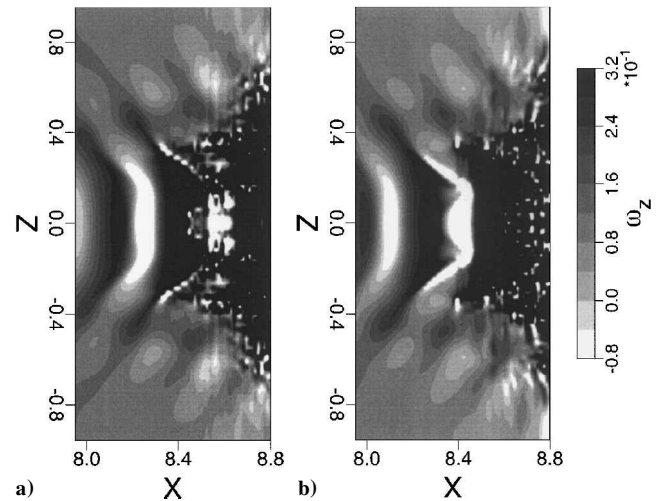


Fig. 12 Iso-areas of total spanwise vorticity ω_z at the wall (\sim wall shear): a) at $t = t_0$ and b) at $t = t_0 + T/2$.

footprints of the structures in the boundary-layer flow (Fig. 12). Very early ($x \sim 8.0$), regions with negative vorticity (white areas) at and close to the wall appear, indicating downstream traveling local separation zones. This had been observed previously for K -type breakdown in a strong APG Falkner–Skan-type boundary layer.^{5,6} The areas of local separation periodically alternate with areas of very high vorticity (black areas) at the wall. The flat center part of the wave front deforms in the transition region and its two bulges at $x = 8.2$, $z = \pm 0.14$ in Fig. 12a accelerate and steepen compared

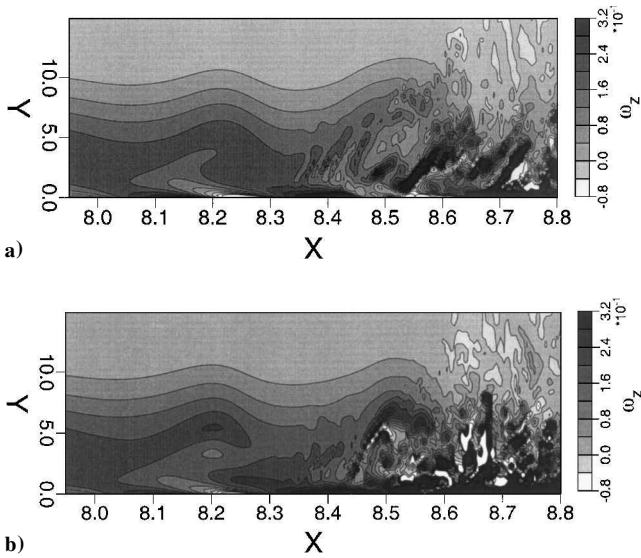


Fig. 13 Iso-areas of total spanwise vorticity ω_z at $t = t_0$ in the x - y plane: a) $z = 0$ and b) off center, $z = 0.19$.

to the surrounding structures, forming a bat-wing-like, \mathcal{M} -shaped contour (dark area between $x = 8.2 \sim 8.4$ in Fig. 12b). This structure could be detected qualitatively also in the experiments.¹⁰

Subsequently, the two peaks of this \mathcal{M} structure divide the negative shear area into a center part (the remainders of which can be found one time period later at $x = 8.6$ in Fig. 12a, however, largely disintegrated) and two “legs” (white “streaks,” $x = 8.4$ and $z = \pm 0.25$). These streaks can be associated with structures inside the boundary layer. They fall back compared to the faster center part and persist for a surprisingly long time embedded in high-shear areas. The upstream ends of these streaks (white spots at $x = 8.4$ and $z = \pm 0.35$; Fig. 12b) remain visible in the flow pattern for one time period longer than the aforementioned structures.

The rapid breakdown of the wave train in this downstream area rather leads to turbulent stripes than to an instant “broad” breakdown region in z . The high-shear area expands in spanwise direction downstream of $x = 8.5$ but the flanks align with the streamwise direction for $x \geq 8.8$ and do not extend abruptly across the entire width of the integration domain.

A streamwise cut through the flowfield at the centerline reveals shear-layer structures reminiscent of the valley plane in ZPG K -breakdown (Fig. 13a; $t = t_0$, mind the stretching of the y coordinate by a factor of 8.7). Distinct shear layers are observed only for $x > 8.48$ (dark areas at an inclination of ~ 45 deg) that intensify on their way downstream, get partially ejected toward outer regions of the flow, and rapid breakdown occurs (compare Fig. 14a half a fundamental time period later, $t = t_0 + T/2$). At the off-center cut at $z = 0.19$ ($z/\lambda_z = 0.1$) a high shear layer formation and development not unlike the peak-plane shear-layer dynamics of K -breakdown can be observed (structure at $x = 8.2$, $y = 5$ in Fig. 13b intensified at $x = 8.36$, $y = 6.5$ in Fig. 14b). At the latter time instance, $t = t_0 + T/2$, an area of high shear close to the wall is also visible, induced by flow reversal (early development can be seen as soon as $x = 8.27$, Fig. 13b at $t = t_0$). Both shear concentrations influence nearby spanwise locations, and their virulent breakup triggers the final laminar breakdown.

A spanwise cut through the flowfield is shown in Fig. 15 at $t = t_0 + T/2$. The discussed ω_z high-shear layers (four concentrations at $z = \pm 0.19$ in Fig. 15a) are strongly localized and enclose a longitudinal vortex structure (ω_x contours in Fig. 15b).

The application of the λ_2 -criterion proposed by Jeong and Hussain¹⁶ reveals further details in the formation and dynamics of vortical structures. The three-dimensional flowfield ($K = 234$) at the preceding time instances were analyzed, and λ_2 isosurfaces are presented in Figs. 16a and 16b at $t = t_0$ and $t = t_0 + T/2$. The distinct formation of a pair of first Λ -vortices, each being asymmetric, can clearly be seen in Fig. 16b. Figure 16a shows a staggered pattern of Λ -vortices, not to be confused with subharmonic breakdown.

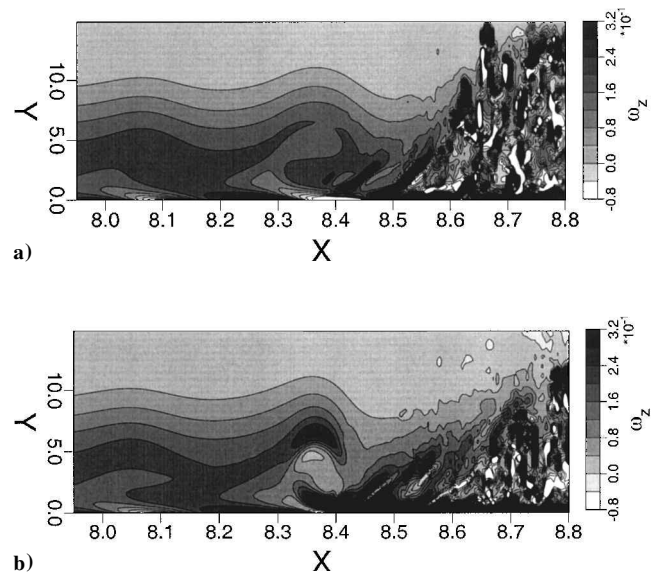


Fig. 14 Iso-areas of total spanwise vorticity ω_z at $t = t_0 + T/2$ in the x - y plane: a) $z = 0$ and b) off center, $z = 0.19$.

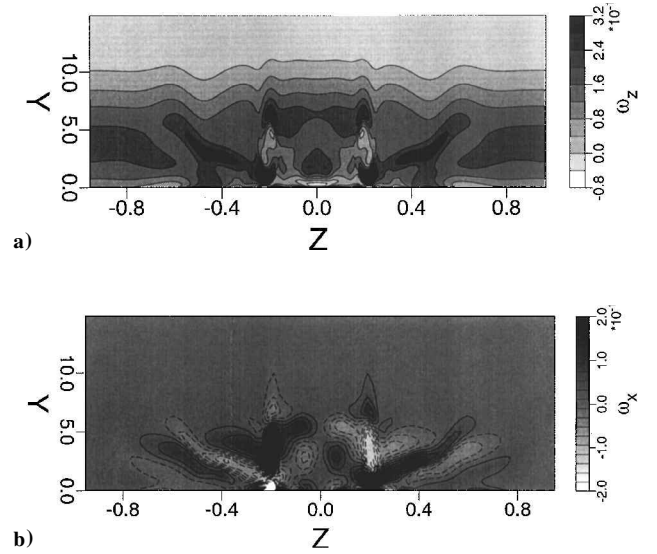


Fig. 15 Iso-areas of vorticity in the y - z plane $x = 8.35$ ($-\lambda_z/2 \leq z \leq \lambda_z/2$, $t = t_0 + T/2$): a) spanwise vorticity ω_z and b) streamwise vorticity ω_x .

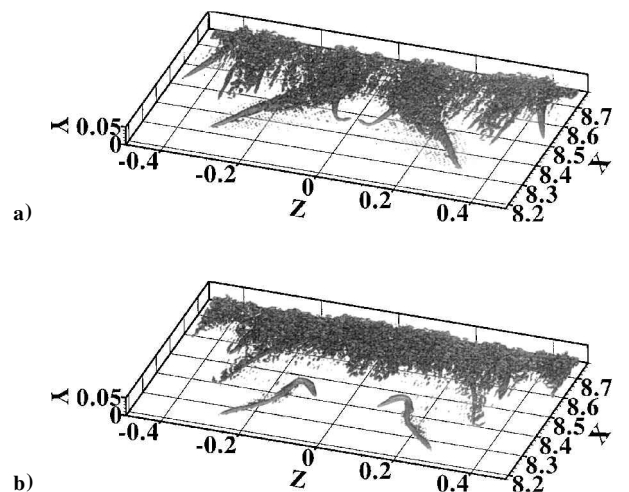


Fig. 16 Visualization of Λ -vortices using the λ_2 -criterion at a) $t = t_0$ and b) $t = t_0 + T/2$ (isosurface representation).

IV. Conclusions

The downstream development of a small-amplitude HPS disturbance in a laminar APG boundary layer has been investigated up to late stages of laminar breakdown by high-resolution DNS.

Detailed investigations of the (wall-)vorticity structures document that the breakdown is neither of the classical fundamental type (K -type) nor of the pure oblique type. A special breakdown involving a multitude of oblique waves with large fundamental three-dimensional mean flow distortion is observed that shows a kind of peak/valley splitting with the valley plane at the centerline of the wave train.

Control DNS with removed or filtered-out two-dimensional wave components clearly show that two-dimensional disturbance modes play no dominant role for the onset of nonlinear mechanisms. Velocity fluctuations are larger for spanwise positions just off-center rather than on centerline, and the major development of vorticity structures takes also place off centerline. Maxima and negative minima (local flow reversal) of the spanwise vorticity ω_z appear at the wall. A clear-cut \mathcal{M} -shaped structure can be observed in final stages related to ω_z at the wall. Inside the boundary layer, close to the boundary-layer edge, areas of high-shear develop where the shear at the wall is at a maximum. It could be shown that the curved HPS wave front does not evolve into a single large-scale Λ -vortex; rather, at first, a pair of asymmetric Λ -vortices in the boundary layer directly evolving from the wave front could be found.

Acknowledgments

The authors wish to express their deepest gratitude to the late Horst Bestek, who initiated this work and gave many helpful suggestions along its path of development. This research has been financially supported by the German Research Council under Contract Be 1192/5-4 and Kl 890/4-1.

References

- ¹Herbert, T., "Secondary Instability of Boundary Layers," *Annual Review of Fluid Mechanics*, Vol. 20, 1988, pp. 487-526.
- ²Thumm, A., "Numerische Untersuchungen zum laminar-turbulenten Strömungsumschlag in transsonischen Grenzschichtströmungen," Doctoral Thesis, Univ. of Stuttgart, Stuttgart, Germany, 1991.
- ³Fasel, H., Thumm, A., and Bestek, H., "Direct Numerical Simulation of Transition in Supersonic Boundary Layers: Oblique Breakdown," edited by L. D. Kral and T. A. Zang, *Transitional and Turbulent Compressible Flows*, Fluids Engineering Div. Vol. 151, American Society of Mechanical Engineers, Washington, DC, 1993, pp. 77-92.

- ⁴Berlin, S., Wiegel, M. and Henningson, D. S., "Numerical and Experimental Investigation of Oblique Boundary Layer Transition," *Journal of Fluid Mechanics*, Vol. 393, Aug. 1999, pp. 23-57.

- ⁵Kloker, M., "Direkte numerische Simulation des laminar-turbulenten Strömungsumschlages in einer stark verzögerten Grenzschicht," Doctoral Thesis, Univ. of Stuttgart, Stuttgart, Germany, 1993.

- ⁶Kloker, M., and Fasel, H., "Direct Numerical Simulation of Boundary-Layer Transition with Strong Adverse Pressure Gradient," *Laminar-Turbulent Transition*, edited by R. Kobayashi, Springer, Berlin, 1995, pp. 481-488.

- ⁷Seifert, A., and Wygnanski, I., "On the Interaction of Wave Trains Emanating from Two Point Sources in a Blasius Boundary Layer," *Proceedings of the Boundary Layer Transition and Control Conference*, Royal Aeronautical Society, Cambridge, England, U.K., 1991, pp. 7.1-7.13.

- ⁸Seifert, A., "Non-Linear Evolution of Point-Source Disturbances in an Adverse Pressure Gradient Laminar Boundary Layer," *Proceedings of the IUTAM Symposium on Nonlinear Instability of 3-D Boundary Layers*, edited by P. W. Duck and P. Hall, Kluwer Academic, Dordrecht, The Netherlands, 1996, pp. 187-196.

- ⁹Suttan, J., Baumann, M., Fühling, S., Erb, P., Becker, S., Lienhart, H., Müller, W., and Stemmer, C., "In-Flight Research on Laminar-Turbulent Transition—A Joint University Research Project," *2nd European Forum on Laminar Flow Technology*, Association Aéronautique et Astronautique de France, Paris, 1996, pp. 10.18-10.41.

- ¹⁰Stemmer, C., Suttan, J., Kloker, M., and Nitsche, W., "Point-Source Induced Transition in Free Flight," *Notes on Numerical Fluid Mechanics*, edited by W. Nitsche and R. Hilbig, Vol. 72, Vieweg Verlag, Wiesbaden, Germany, 1999, pp. 458-465.

- ¹¹Kloker, M., Konzelmann, U., and Fasel, H., "Outflow Boundary Conditions for Spatial Navier-Stokes Simulations of Transition Boundary Layers," *AIAA Journal*, Vol. 31, No. 4, 1993, pp. 620-628.

- ¹²Rist, U., and Fasel, H., "Direct Numerical Simulation of Controlled Transition in a Flat-Plate Boundary Layer," *Journal of Fluid Mechanics*, Vol. 298, Sept. 1995, pp. 211-248.

- ¹³Stemmer, C., Kloker, M., and Wagner, S., "DNS of Harmonic Point Source Disturbances in an Airfoil Boundary Layer," *AIAA Paper 98-2436*, June 1998.

- ¹⁴Gilyov, V. M., Kachanov, Y. S., and Kozlov, V. V., "Development of a Spatial Wave Packet in a Boundary Layer," *Izvestiya Sibirskovo Otdeleniya Akademii Nauk SSSR, Seria Tekhnicheskikh Nauk*, Vol. 3, No. 13, 1983, pp. 27-37 (in Russian).

- ¹⁵Mack, L. M., and Herbert, T., "Linear Wave Motion from Concentrated Harmonic Sources in Blasius Flow," *AIAA Paper 95-0774*, Jan. 1995.

- ¹⁶Joeng, J., and Hussain, F., "On the Identification of a Vortex," *Journal of Fluid Mechanics*, Vol. 285, Feb. 1995, pp. 69-94.

P. Givi
Associate Editor